# Structure and organization of full-length epidermal growth factor receptor in extracellular vesicles by cryo-electron tomography

Monica Gonzalez-Magaldi[a] (ID), Anuradha Gullapalli[a] (ID), Ophelia Papoulas[a] (ID), Chang Liu[a], Adelaide Y.-H. Leung[a] (ID), Luqiang Guo[a], Axel F. Brilot[b] (ID), Edward M. Marcotte[a] (ID), Zunlong Ke[a,c,1] (ID), and Daniel J. Leahy[a,1] (ID)

We report here transport of full-length epidermal growth factor receptor (EGFR), Insulin Receptor, 7-pass transmembrane receptor Smoothened, and 13-pass Sodium-iodide symporter to extracellular vesicles (EVs) for structural and functional studies. Mass spectrometry confirmed the transported proteins are the most abundant in EV membranes, and the presence of many receptor-interacting proteins in EVs demonstrates their utility for characterizing membrane protein interactomes. Cryo-electron tomography of EGFR-containing EVs reveals that EGFR forms clusters in both the presence and absence of EGF with a ~3 nm gap between the inner membrane and cytoplasmic density. EGFR extracellular region (ECR) dimers do not form regular arrays in these clusters. Subtomogram averaging of the 150 kDa EGF-bound EGFR ECR dimer yielded a 15 Å map into which the crystal structure of the ligand-bound EGFR ECR dimer fits well. These findings refine our understanding of EGFR activation, clustering, and signaling and establish EVs as a versatile platform for structural and functional characterization of human membrane proteins in cell-derived membranes.

EGFR | cryo-ET | subtomogram averaging | extracellular vesicles | mass spectrometry

Structural studies of soluble fragments or detergent-solubilized forms of integral membrane proteins have yielded substantial insight into diverse biological processes (1–3). For example, crystal structures of the extracellular region (ECR) of the epidermal growth factor receptor (EGFR), a Receptor Tyrosine Kinase composed of a ligand binding ECR, a single transmembrane region (TM), and an intracellular kinase domain, revealed a large domain rearrangement in the ECR when ligand is bound (4–7). This rearrangement exposes buried surfaces that mediate formation of EGFR ECR dimers that promote formation of an asymmetric dimer of intracellular kinase regions that stimulates kinase activity and is essential for signaling (8, 9).

These observations are consistent with the long-held model that EGFR is activated by ligand-dependent dimerization (10) but fail to explain all aspects of EGFR behavior. For example, EGFR has been shown to form multimers in the absence of ligand (11–18) and higher-order oligomers in the presence of ligand (19–21). In addition, distinct EGFR ligands stimulate different cellular responses in otherwise similar conditions (22–24). This phenomenon, known as biased agonism, has been attributed to different ligands modulating EGFR ECR dimer structure in a way that is communicated to the intracellular kinase (25–27) and to different ligand binding and EGFR dimerization kinetics for different ligands (28).

Understanding whether or how the EGFR ECR communicates structural information to the intracellular region (ICR) beyond dimerization and the nature and importance of noncanonical EGFR oligomers would be greatly aided by visualization of intact forms of EGFR. Several recent studies have used single-particle cryo-electron microscopy (cryo-EM) to examine full-length or near full-length forms of EGFR or EGFR homologs solubilized in detergents, nanodiscs, or peptidiscs (27, 29, 30). These studies have revealed ordered ECR dimers that are largely consistent with crystal structures, but considerable flexibility between ECRs and ICRs precluded resolution of ICR structures. It is not clear whether this flexibility is an intrinsic feature of EGFR or a consequence of solubilization methods.

Recent cryo-electron tomography (cryo-ET) and single-particle cryo-EM studies of proteins on viral envelope surfaces (31, 32), in liposomes (33), organelles (34), synaptic vesicles (35), or sonication-induced or homogenized vesicles (35, 36) have resulted in subnanometer and near-atomic resolution structures, respectively, demonstrating the potential for structural studies of membrane proteins in vesicles. To enable structural

## Significance

We show that transporting integral membrane proteins to cell-derived extracellular vesicles is a straightforward approach that enables structural and functional studies of human proteins in a membrane environment. We have used this approach to visualize full-length epidermal growth factor receptor (EGFR) and show that it forms clusters in the membrane and projects its cytoplasmic signaling domains ~3 nm away from the membrane surface. EGFR is essential for normal development, but abnormal EGFR activity is associated with several human cancers and is the target of many anticancer therapies. Our studies refine current models of how ligand binding to EGFR transmits signals across cell membranes.

and functional studies of EGFR and other integral membrane proteins in cell-derived membranes we developed a system to transport human membrane proteins to Virus-like Particles (VLPs). VLPs are noninfectious enveloped viral particles ~60 to 150 nm in diameter that bud off from cell membranes and whose membranes are enriched in viral proteins (37, 38). We were able to produce VLPs containing EGFR by cotransfecting a gene encoding EGFR with an N-terminal epitope tag, a gene encoding a viral surface protein fused to an epitope binding module, and the Murine Leukemia Virus (MLV) Gag protein into HEK 293T cells. To demonstrate that multipass integral membrane proteins may also be transported to VLPs by this approach, we found that the Insulin Receptor (InsR, 2-pass), Smoothened (Smo, 7-pass), and the Sodium-iodide symporter (NIS, 13-pass) are also transported to VLPs.

In the midst of this work, Hoffmann, Bjorkman, and colleagues reported that appending a 110 amino acid sequence containing binding regions for Endosomal Sorting Complex Required for Transport (ESCRT) and ALG-2 interacting protein X (ALIX) proteins to the severe acute respiratory syndrome coronavirus 2 (SARS-CoV-2) spike protein resulted in formation of spike-containing virus-like vesicles they term enveloped VLPs (39). We find that appending this ESCRT and ALIX binding region (EABR) to EGFR or other human single- and multipass integral membrane proteins results in production of vesicles containing the EABR-labeled protein when expressed as a single protein in Expi293F cells. As these vesicles contain no viral proteins, we will refer to them as extracellular vesicles (EVs).

Using EGFR as an example, we show that EVs are a simplified and advantageous system for structural and functional studies of human membrane proteins in cell-derived bilayers. Mass spectrometric analysis of EGFR-containing EVs shows enrichment in many known EGFR-interacting proteins, demonstrating that EVs can be used to characterize membrane protein interactomes, analogous to the Virotrap approach for cytoplasmic proteins (40). As many of these enriched proteins bind to phosphorylated EGFR, the process of EV formation appears to have led to EGFR activation despite the absence of added ligand. Cryo-ET analyses of EGFR-containing EVs in the presence of excess EGF reveal that EGFR forms clusters in EV membranes but that the EGFR ECRs do not form regular contacts in these clusters. A ~3 nm gap is also observed between the inner membrane surface and cytoplasmic density indicating that EGFR kinase domains are projected away from the membrane in the active state. Subtomogram averages of the 150 kDa EGFR ECR dimer resulted in 15 Å density maps into which the crystal structure of dimer of the EGFR-ECR:EGF complex fits well. Cryo-ET analyses of EGFR-containing EVs to which EGF was not added reveal smaller ECR particles consistent with the unliganded EGFR ECR (4). These particles also form clusters with a ~3 nm gap between the inner membrane surface and cytoplasmic density that may stem from activation of EGFR during EV formation.

## Results

**Transport of Human Membrane Proteins to VLPs.** To create molecules that bind epitope-tagged proteins of interest and transport them to VLPs, Strep-tactin (SA) and single-chain Fv (scFv) fragments of antibodies that recognize Hemagglutinin (HA) (41) or FLAG (42) peptides were substituted for the ECR of Influenza Neuraminidase (*SI Appendix,* Fig. S1). To allow for simple detection of these molecules, which we term "transporters," and increase accessibility of the scFv regions to epitopes on target proteins, glycine-serine (Gly-Ser) linkers and tandemly repeated myc tags were inserted between Neuraminidase and scFV

sequences, and a triple repeat of FLAG sequences was inserted between Neuraminidase and SA. A rhinovirus 3C protease recognition site was also added to the juxtamembrane region of each transporter to enable proteolytic removal of ECRs after VLP formation (*SI Appendix,* Fig. S1). Each of the HA, FLAG, and SA transporters expressed well in CHO and HEK293 cells and led to VLP formation from HEK 293T cells when cotransfected with a gene encoding the MLV Gag protein (*SI Appendix,* Fig. S1) (43).

Initial purification and concentration of VLPs was achieved by centrifuging VLP-containing media through a 20% sucrose cushion and resuspension of the VLP-containing pellet. When coexpressed with a gene encoding human EGFR with a cognate epitope tag on its N terminus, each transporter mediated transport of EGFR to VLPs (*SI Appendix,* Fig. S1). Cryo-electron micrographs of EGFR-containing VLPs showed the presence of membrane-associated particles with size consistent with EGFR in the majority of VLPs, with empty VLPs presumably arising from cells expressing Gag but not EGFR proteins. Addition of Rhinovirus 3C protease to VLPs resulted in cleavage of both the transporter ECRs and the N-terminal epitope tags on EGFR (*SI Appendix,* Fig. S3), leaving EGFR behind as the most abundant membrane protein with sizeable extra- and intracellular regions. These transporters transported tagged but not untagged proteins to VLPs produced in HEK 293T cells (*SI Appendix,* Fig. S4). When untagged EGFR was expressed in Expi293F cells at ~sixfold higher levels than HEK 293T cells, however, the transporter was not needed for EGFR to enter VLPs suggesting that transporters and epitope tags may not be needed if the target protein expresses at high levels, consistent with prior results producing vesicles from cells overexpressing proteins (36, 44) (*SI Appendix,* Fig. S4).

**EABR Tags Target Human Membrane Proteins to EVs.** Hoffmann, Bjorkman, and colleagues recently reported that addition of a 110 amino acid segment containing EABR to the C-terminus of the SARS-CoV-2 spike protein resulted in exocytosis of spike-containing vesicles (39). We appended the EABR sequence, which also contains an endocytosis prevention motif (45), to the cytoplasmic termini of the SA and HA transporter proteins, EGFR, InsR, the 7-pass transmembrane receptor Smo, and the 13-pass transmembrane NIS and observed transport of each molecule to EVs when transfected into Expi293F cells (Fig. 1 and *SI Appendix,* Fig. S1). Addition of EABR to the C-terminus of EGFR and InsR did not inhibit their activation as judged by anti-phosphotyrosine Western blots (*SI Appendix,* Fig. S5). The ability of the EABR-based transporter and EABR-labeled EGFR to produce and enter EVs (Fig. 2) indicates that the EABR tag is effective in both orientations relative to the membrane and when separated from the TM region by greater than 500 amino acids.

**Purification and Characterization of EVs.** Initial purification of EVs from conditioned medium by centrifugation through a 20% sucrose cushion led to recovery of EVs as judged by western blot and cryo-EM, but the micrographs indicated the presence of sufficient levels of contaminants to complicate electron-microscopic studies. A Strep-Tag II sequence (46) followed by a rhinovirus 3C protease recognition site (47) was thus added to the N terminus of EABR-labeled EGFR, and EGFR-containing EVs further purified using a SA affinity resin (Fig. 1) (48). This affinity-purification step yielded EGFR-containing EVs of sufficient purity for cryo-electron microscopic studies (Fig. 2*C*) and was also used to purify InsR-, Smo-, and NIS-containing EVs (*SI Appendix,* Fig. S2).

Intensity-based abundance quantification (iBAQ) (49, 50) of mass spectrometric results obtained from EGFR-containing EVs following affinity purification indicate that the mole fraction of
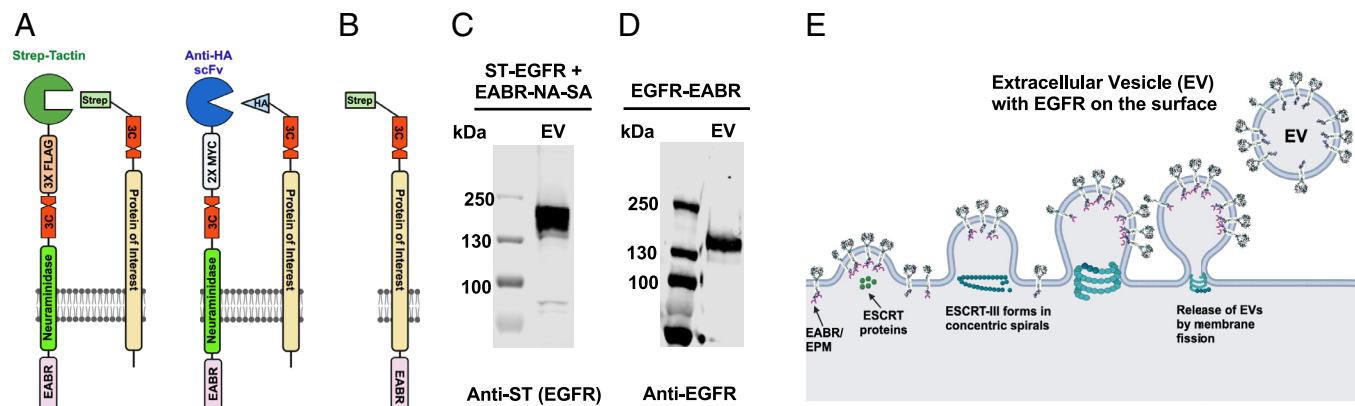
**Fig. 1.** Transport of human proteins to EVs. (A) Schematic diagram of "transporter" proteins containing the EABR fused to the N-terminal region of influenza neuraminidase followed by a peptide binding module. (B) Schematic diagram of a protein of interest with the EABR fused to its C-terminus to promote transport to EVs and a Strep-tag II epitope fused to its N terminus to enable purification of EVs using a SA affinity column. (C) Western blot analysis of affinity-purified EVs derived from Expi293F cells transfected with the SA transporter diagrammed in (A) along with Strep-tag II (ST) labeled EGFR. (D) Western blot analysis of affinity-purified EVs derived from Expi293F cells transfected with EABR-tagged EGFR. The probing antibody is indicated below each blot. (E) Cartoon representation of EV formation stimulated by expression of EABR-labeled EGFR.

EGFR in EV membranes is 62% (Fig. 2D). The ECRs of each of the seven next most abundant membrane proteins, which represent >20% of the mole fraction EV membrane proteins, are <20 kDa indicating EGFR ECRs represent >80% of extramembrane particles visible in electron micrographs. In addition, many proteins known to interact with EGFR intracellular regions were enriched in EGFR-containing EVs relative to non-EGFR-containing EVs (Fig. 2E and Dataset S1). Many of these enriched proteins, including Grb2, Shc1, PLCγ1, Cbl, and PI3K, bind phosphorylated EGFR suggesting that EGFR overexpression or clustering during EV production led to ligand-independent activation (51). Indeed, western blot analysis of purified EGFR-containing EVs showed basal phosphorylation of EGFR that increased following addition of EGF (SI Appendix, Fig. S5).

**Cryo-ET of EGFR in EVs.** EGF was added to EGFR-containing EVs prior to addition to electron microscope grids and plunge-freezing in liquid ethane. Tomograms were calculated from tilt series collected on a Titan Krios equipped with a Gatan K3 detector and Biocontinuum energy filter. Tomograms revealed EVs with diameters of $88 \pm 26$ nm and surface particles of the size and shape expected for ligand-bound EGFR ECR dimers (Fig. 3 and SI Appendix, Figs. S6 and S8). Lower resolution in the z-direction complicates particle identification away from the x-y plane, but particle counts from 10 EVs selected from two of the best tomograms and ranging between 62 and 142 nm in diameter resulted in a scaled average of $110 \pm 42$ dimers per 100 nm diameter vesicle or $\sim 3,500 \pm 1,340$ dimers per $\mu m^2$. Assuming that physiological concentrations of EGFR are on the order of ~100 receptors/$\mu m^2$ (52), or ~3 EGFRs per 100 nm diameter EV, EGFR concentrations in EVs are 20- to 50-fold above physiological concentrations.

Visualization of whole EVs from tomograms can be challenging due to distortions arising from EVs abutting the edge of grid holes and from the "missing wedge" of data, which leads to poorer resolution in the direction perpendicular to the plane of the EM grid. The program ISONET (53) was thus used to compensate for missing wedge effects and reconstruct an isotropic view of EVs for a set of EVs entirely contained in vitreous ice (Fig. 3 A–C). EGFR dimers generally appear in clusters with a ~3 nm gap between the intracellular membrane and intracellular density in both reconstructed and unreconstructed tomograms (Fig. 3). Individual EGFR dimers are occasionally observed onto which

the crystal structure of the EGFR:EGF complex dimer can be placed and with intracellular density consistent with the asymmetric EGFR kinase dimer projected ~3 nm from the inner membrane surface (Fig. 3 E–H and SI Appendix, Fig. S9).

To examine the arrangement of EGFRs in clusters, tomographic sections in which cross-sections of EGFR clusters are present were inspected. These sections show irregular arrangements of EGFR ECRs (Fig. 4). Although isolated EGFR ICRs are occasionally observed, the ICRs of EGFRs in clusters are generally part of an amorphous assembly of density projected ~3 nm below the inner membrane. To characterize this density, pie-shaped regions of a two-dimensional section of an EV tomogram were selected that either contained a cluster of EGFR:EGF complexes or were receptor-free. The radial density of these regions was averaged and confirms accumulation of cytoplasmic density underneath EGFR clusters and the presence of a ~3 nm gap between the inner membrane and EGFR cytoplasmic region (Fig. 5A). Subtomogram averages of volumes from regions of four comparably sized EVs that either contain a cluster of EGFR:EGF complexes or are receptor-free also demonstrate a concentration of cytoplasmic density at sites of EGFR clusters that is separated from the inner membrane by ~3 nm (Fig. 5 B–D).

The 31 amino acid EGFR juxtamembrane region contains an N-terminal 21 amino acid segment (Juxtamembrane-A or JMA) and a C-terminal 10 amino acid segment (Juxtamembrane-B or JMB) also called the "latch" because it forms an extended contact with another kinase in the active asymmetric EGFR kinase dimer (54, 55). If the JMA region adopts a random coil structure, it would likely not be rigid enough to project the EGFR kinase domains 3 nm away from the membrane. We thus believe the best explanation for this gap is that the JMA region forms a homodimeric parallel coiled-coil-like structure, which would extend almost exactly 3 nm for a sequence of this length. Such a structure is predicted by AlphaFold 3 for a homodimer of the EGFR transmembrane and juxtamembrane regions (SI Appendix, Fig. S10) (56).

To determine whether the observed clustering of EGFR dimers is a consequence of ligand binding, tomograms of EGFR-containing EVs to which EGF was not added were calculated. These tomograms revealed extracellular particles of a size and shape expected for unliganded EGFR monomers (SI Appendix, Fig. S7) (4). These particles also appear in clusters indicating that the clusters observed in the presence of EGF are not solely ligand dependent. Radial density analysis also reveals a ~3 nm gap between the membrane
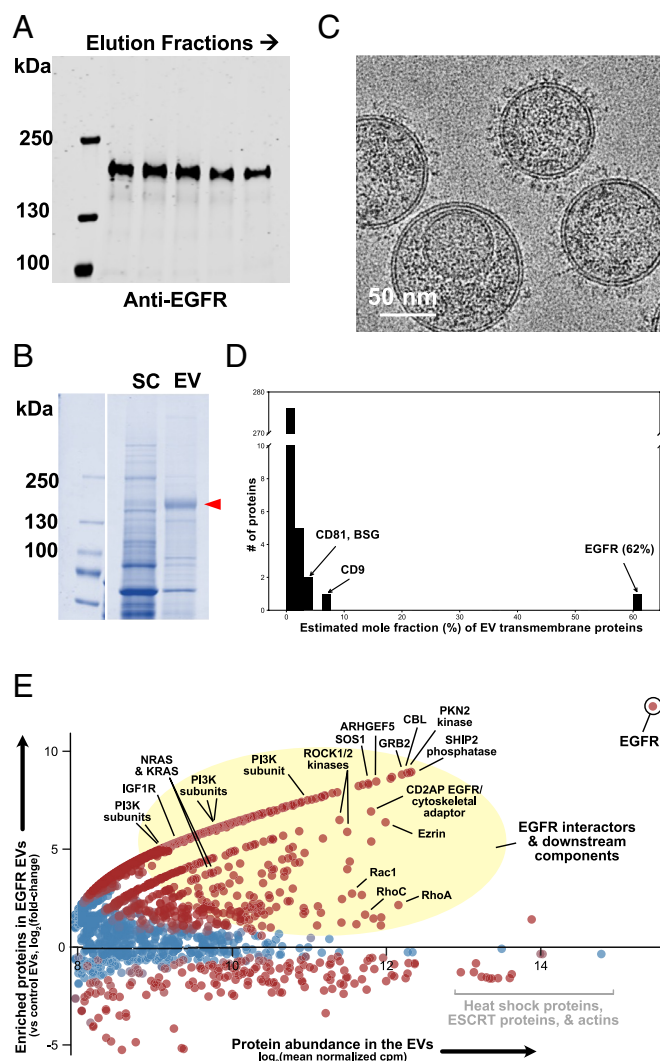
**Fig. 2.** Affinity purification and characterization of EGFR-containing EVs. (*A*) Anti-EGFR western blot of EGFR-containing EVs eluted from a SA column. (*B*) Coomassie Blue stained Sodium Dodecyl Sulfate Polyacrylamide Gel Electrophoresis analysis of affinity-purified EGFR-containing EVs. EGFR is indicated by a red arrowhead. (*C*) Cryo-electron micrograph of affinity-purified EGFR-containing EVs. (*D*) Mass spectrometric riBAQ analysis of mole fractions of transmembrane proteins in affinity-purified EGFR-containing EVs. (*E*) Plot of the log(Fold-change) (logFC) in the mass spectrometric counts of all proteins in EVs produced by transfection with EGFR-EABR relative to EVs without EGFR. The position of EGFR is indicated along with the positions of several proteins known to be involved in EGFR signaling. A full list of abbreviations and interacting proteins can be found in *SI Appendix*.

and intracellular density (*SI Appendix,* Fig. S11). The presence of clusters and the gap may stem from the fact that EGFR becomes activated during EV formation (Fig. 2 and *SI Appendix,* Fig. S5).

The appearance of recognizable EGFR ECR dimers in tomograms of EGFR-containing EVs led us to try structure determinations by both single-particle and subtomogram averaging. Initial attempts to determine the EGFR ECR structure by single-particle averaging of particles picked from cryo-EM projection images failed, however, which may stem from the overlap of multiple receptors in projection images of EGFR clusters. We thus focused our efforts on subtomogram averaging and were able to generate a 15 Å map of the EGFR ECR from 843 of 1,602 manually picked particles from 20 tomograms with 2 to 10 EVs per tomogram (Fig. 6*A* and *SI Appendix,* Fig. S12). These maps, on which C2 symmetry was imposed but otherwise used no template information from prior structures, faithfully reproduce features of the EGFR:EGF ECR

crystal structure [RCSB 3NJP (57)] with the addition of bulges at sites of N-linked glycosylation (Fig. 6*A*). Examination of subtomogram average classes from rejected particles fails to reveal classes in which the domain IV "legs" exhibit movements observed in a cryo-EM structure of EGFR in peptidiscs (27) and molecular dynamics simulations (58), which may indicate that the presence of the bilayer membrane stabilizes the EGFR ECR domain IV position observed in crystal structures (57).

Owing to the scarcity of isolated EGFRs in EV membranes, the merging of intracellular density within EGFR clusters, and the likely association of EGFR interaction partners with EGFR ICRs, it proved difficult to identify well-defined and circumscribed EGFR ICR density. Sixteen such ICRs were identified, however, and when averaged produced a map consistent with the EGFR asymmetric kinase dimer (8) with a ~3 nm stalk connecting it to the inner membrane surface (Fig. 6*C*).

## Discussion

To enable structural and functional studies of intact integral membrane proteins in cell-derived membranes we developed a system for transporting epitope-tagged human membrane proteins to VLPs by attaching epitope binding modules to portions of viral surface proteins naturally transported to viral membranes. Appending the 110 amino acid EABR sequence described by Hoffman, Bjorkman, and colleagues to EGFR or cotransfection of EABR-tagged epitope binding modules with epitope-tagged EGFR both led to efficient production of EVs containing EGFR (39). Appending the EABR tag to the C termini of the Insulin Receptor, the 7-pass transmembrane protein Smo, and the 13-pass transmembrane protein NIS also results in EV production, indicating this approach is effective for multipass as well as single-pass membrane proteins. The EABR tag has the advantages that cotransfection with viral genes is not needed to produce vesicles and that virtually all EVs contain the desired protein. The epitope-binding module system has the advantages that any effects of the EABR tag on the target protein are avoided and the concentration of the desired protein may be modulated independently of EV production.

Cryo-ET and mass spectrometric analyses of EGFR-containing EVs indicate that EGFR represents at least 80% and likely more of the ECR particles visible in electron micrographs (49), which simplifies particle identification in low-resolution cryo-electron tomograms (57). EGFR particles generally occur in clusters, but the EGFR ECRs do not form regular interactions. Several non-mutually exclusive causes may underlie cluster formation including: normal physiological interactions, crosslinking by effector proteins, association with ESCRT proteins, or the abnormally high concentration of EGFR in EVs.

To test whether the clusters are a feature of ligand-bound EGFR, we generated tomograms of EGFR-containing EVs to which EGF had not been added. The size of the ECR particles in these EVs is consistent with unliganded EGFR ECR monomers, but unliganded EGFR also appears in clusters. As both western blotting and mass spectrometric data indicate that EGFR becomes phosphorylated during EV production despite the absence of ligand, clusters of unliganded EGFR in EVs may stem from this activation. Future experiments will be needed to sort out the causes and physiological relevance of EGFR cluster formation.

An unexpected feature of EGFR clusters is the presence of a ~3 nm gap between the inner membrane and a layer of intracellular density that is occasionally spanned by weak tubes of density opposite EGFR ECRs. The JMA region of active EGFR dimers
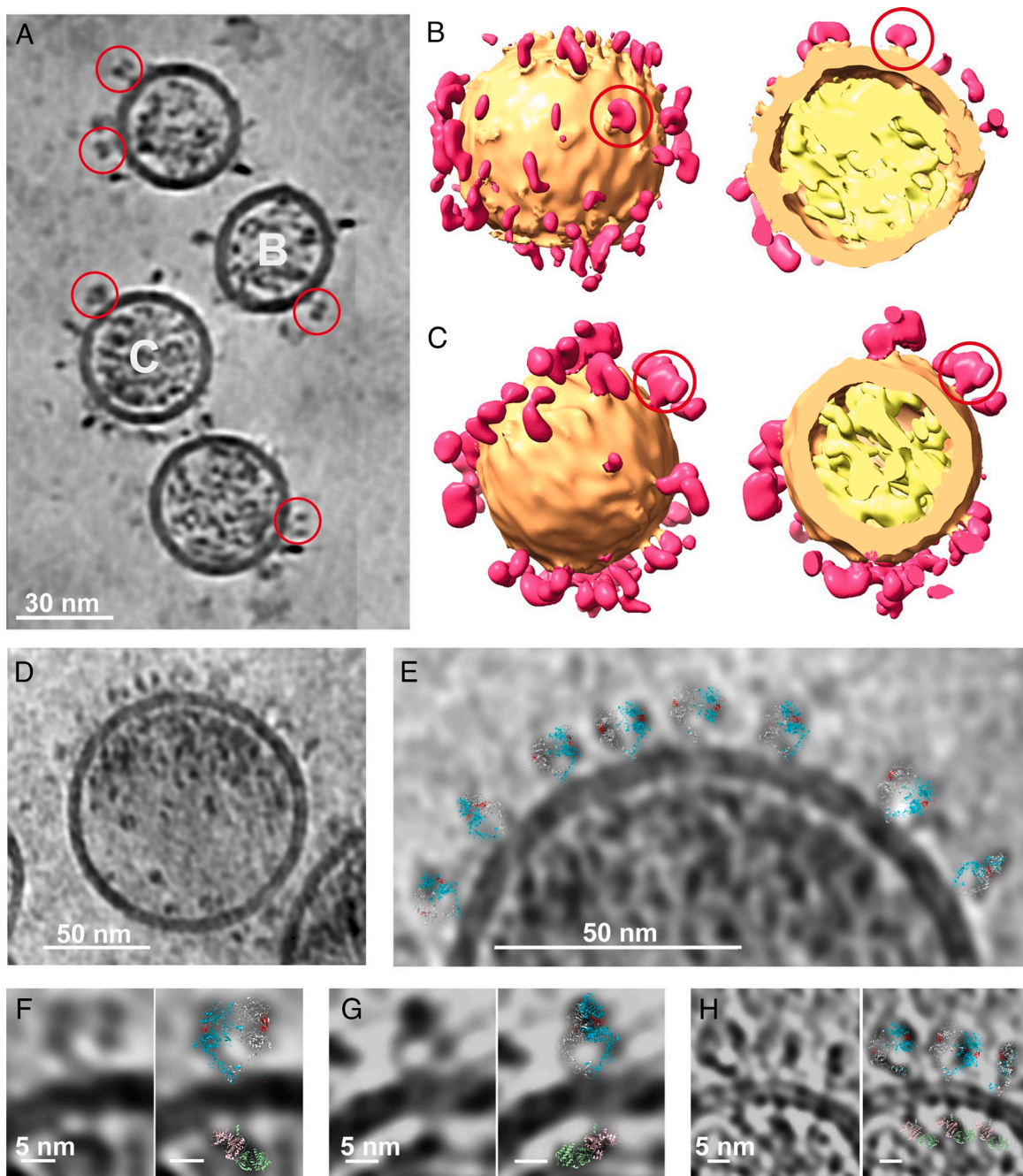
**Fig. 3.** Tomograms of EGFR-containing EVs. (*A*) Section of a tomogram of EGFR-containing EVs following application of ISONET to compensate for the missing wedge. Individual EGFR ECRs circled in red. (*B* and *C*) Enlarged views of two EVs from panel *A* showing the ECR (pink), membrane (tan), and intracellular region (yellow). Several EGFR ECRs are circled in red. (*D*) A section of a tomogram of an EGFR-containing EV is shown. (*E*) An enlarged region of the tomographic section shown in panel *D* is shown with ribbon diagrams of the EGFR ECR dimer (RCSB 3NJP; EGF is colored red and the EGFR subunits are colored cyan and light gray) manually positioned in the tomogram. (*F–H*) Images of individual EGFR molecules from tomograms of EGFR-containing EVs are shown alongside the same image with the crystal structures of the EGFR ECR dimer colored as in panel *E* and the asymmetric EGFR kinase dimer (RCSB 3GOP; one kinase subunit is colored light pink and the other light green).

has been predicted to form an antiparallel coiled-coil based on NMR data (26), but such a structure could not explain the 3 nm gap we observe. We believe that the best explanation for the 21 amino acid JMA region stably and rigidly projecting the EGFR kinase domains 3 nm away from the membrane is formation a homodimeric parallel coiled-coil-like structure. Such a structure is predicted for the transmembrane and juxtamembrane regions by AlphaFold 3 (56). If a feature of inactive EGFR is separation of the TM regions (52), an antiparallel coiled-coil of JMA regions may be favored in this state. The ~3 nm gap we observed between the membrane and intracellular density for unliganded EGFR

seems likely to stem from the ICR adopting an active conformation during EV formation, which likely involves formation of the asymmetric kinase dimer and promotion of the coiled-coil conformation of the juxtamembrane region.

The observation of this gap raises the question of what its functional role might be. One possibility is suggested by the electrostatic model of EGFR activation in which interactions between a positively charged surface of the EGFR kinase and the negatively charged inner membrane surface inhibit EGFR activity in the absence of ligand and activation of the kinase requires release from the membrane (59). Formation of a coiled-coil by the JMA region
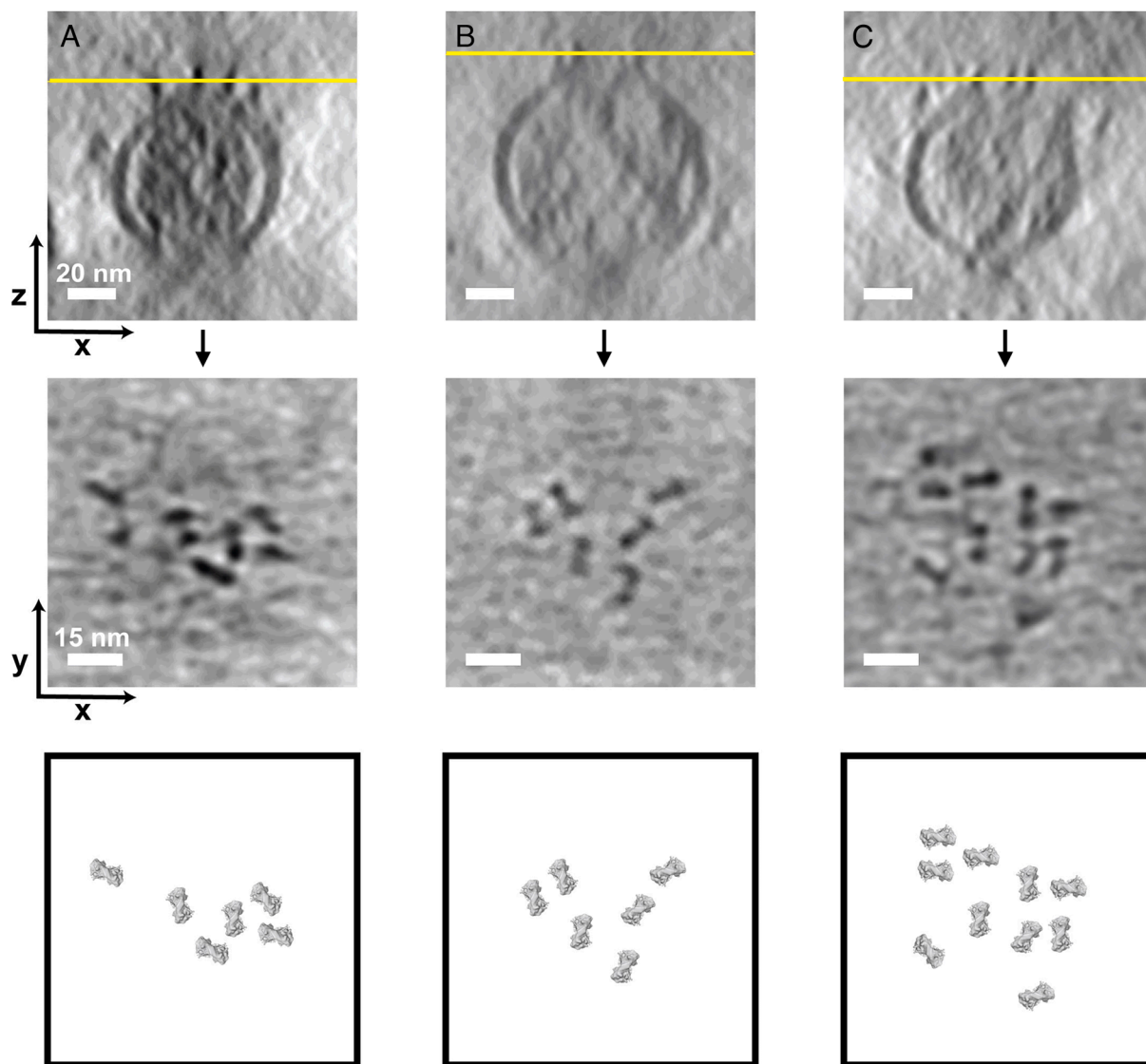
**Fig. 4.** The ECRs of clustered EGFRs do not form regular arrays. (*Top*) Tomographic sections of three different EVs (*A–C*) fully embedded in ice, viewed perpendicular to the plane of the EM grid. Yellow lines indicate the approximate positions of the corresponding x-y planes shown below each section in the *Middle* panels. (*Middle*) Tomographic sections of the same tomograms in the *Top* row but viewed in the plane of the EM grid near the edges of the EVs. (*Bottom*) Top–down views of cross-sections of the EGFR dimer derived from the crystal structure (RCSB: 3NJP), which are bowtie-shaped and ~4.5 × 11 nm, positioned as in the *Middle* panels.

in active EGFR dimer may thus be a mechanism to release inhibitory interactions between the EGFR kinase and the inner membrane surface. Support for this model comes from the observation that when the EGFR intracellular region was targeted to the inner membrane surface by a myristoylation signal it was not highly active unless a GCN4 coiled-coil region was inserted between the myristoylation site and the kinase region with the objective of forcing dimerization and disrupting interactions between the kinase domain and membrane (26). Insertion of a GCN4 zipper in this case may have led to kinase activation by mimicking the structure and role of the JMA region in active EGFR.

Although cryo-electron microscopic studies of membrane proteins in various vesicles and organelles have reached subnanometer and near atomic resolution for tomographic and single particle studies, respectively, these studies have involved lattice forming proteins or proteins greater than 0.5 MDa (34–36, 60–62). It was thus not clear that comparable resolutions could be obtained for proteins as small as the ~150 kDa EGFR ECR dimer and its ~72 kDa intracellular kinase dimer. Indeed, our attempts to produce single-particle averages of EGFR ECRs from projection images

of EGFR-containing EVs have failed so far, presumably owing in part to overlap of adjacent receptors in projection images. 3D Tomograms of EGFR-containing EVs contain recognizable EGFR ECRs that are separable, however, and subtomogram averages of 843 particles yields a density map with 15 Å resolution by the 0.143 FSC criterion. The crystal structure of the EGF-bound EGFR dimer fits into this map extremely well (Fig. 6), indicating that crystal structures of isolated EGFR ECRs are an accurate reflection of the dominant conformation of EGFR ECRs in intact receptors in membrane bilayers and that the resolution obtained here is sufficient to allow placement of domains of known structure into experimental maps.

The absence of additional density surrounding the EGFR ECR in subtomogram averages is consistent with EGFR ECRs not forming a conserved interdimer interaction. Had a specific higher-order contact between EGFR ECR dimers been prevalent, density reflecting this contact would have appeared in our subtomogram averages. Bulges in density do occur, but they are invariably at sites of N-linked glycosylation. We also do not observe flexibility in the disposition of the domain IV relative to domain
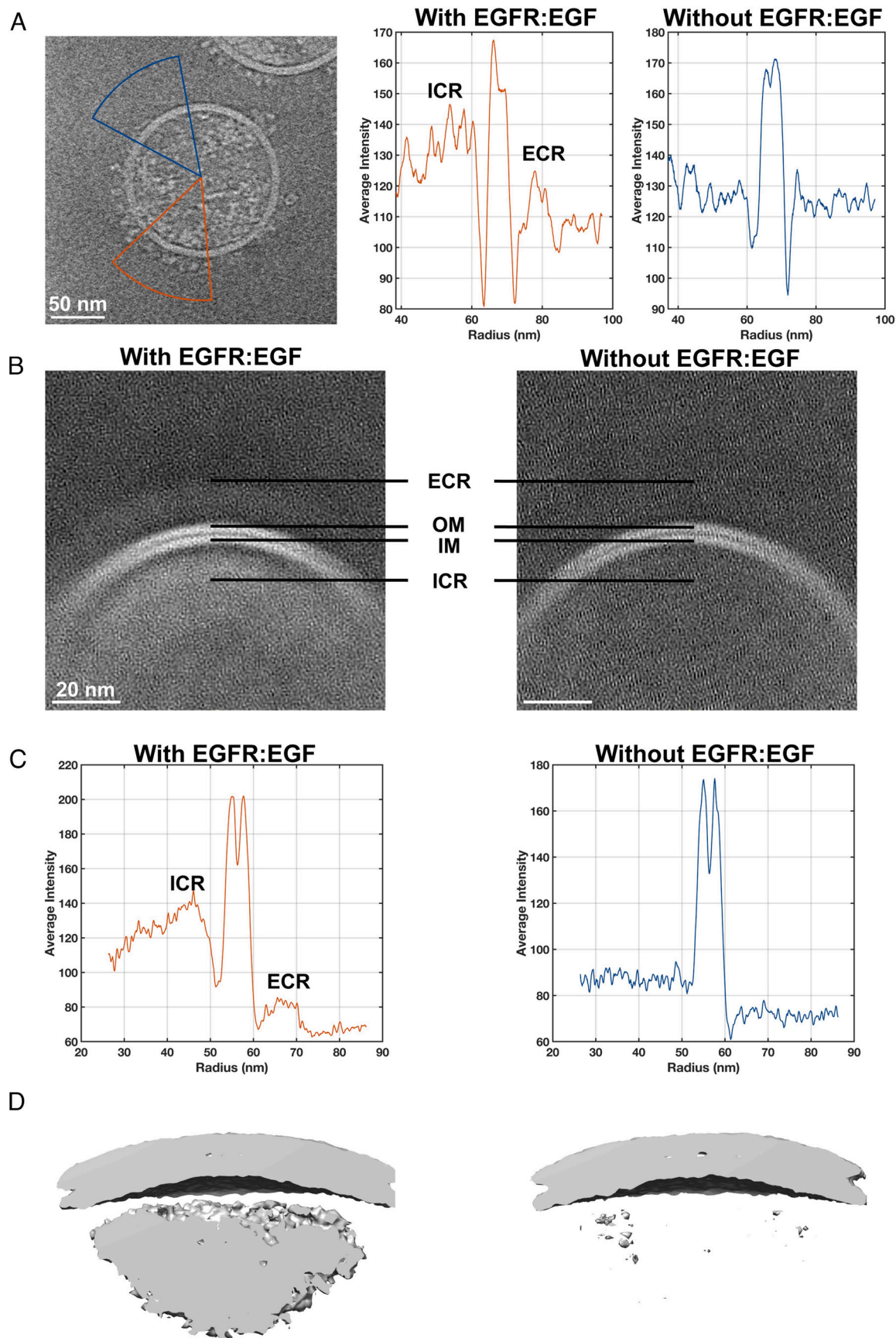
**Fig. 5.** Characterization of intravesicular density. (*A*) 2D tomographic section (*Left*) of an EGFR:EGF-containing EV showing regions with (orange) and without (blue) an EGFR cluster. The average radial density of these regions is shown in the *Middle* and *Right* panels. (*B*) 2D sections of a 3D subtomogram average of regions of four comparably sized EVs that contain EGFR:EGF (*Left*) or are devoid of EGFR:EGF (*Right*). The ECR, outer membrane (OM), inner membrane (IM), and ICR are indicated. Averaged radial density (*C*) and isosurface view (*D*) of the subtomogram averages shown in panel *B*.
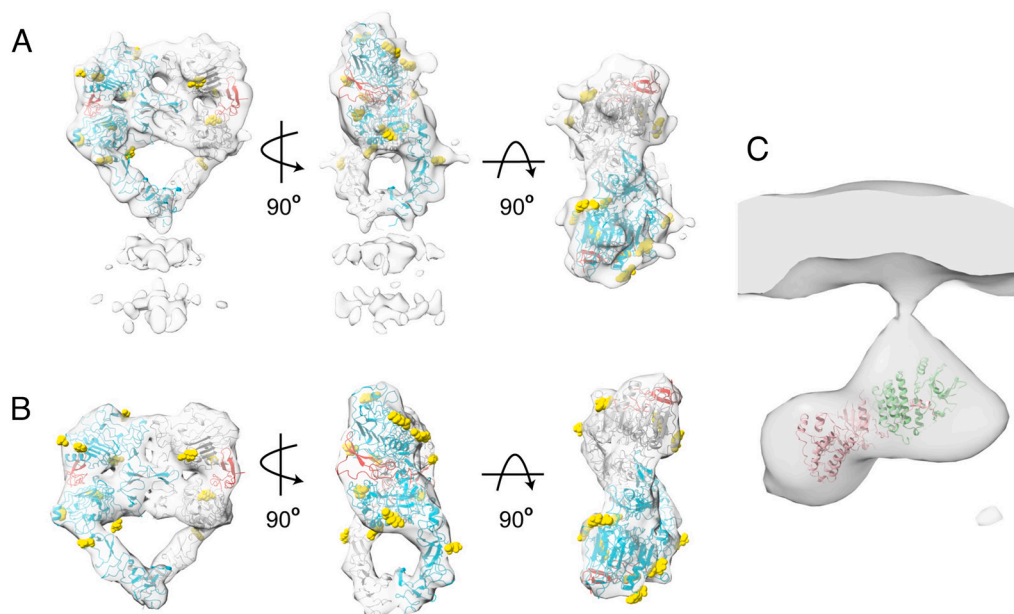
**Fig. 6.** Subtomogram averages of the EGFR:EGF ECR in EVs strongly resemble the crystal structure. (*A*) Orthogonal views of the crystal structure of a dimer of the EGFR ECR complexed with EGF (RCSB 3NJP; the EGFR subunits are colored cyan and light gray and EGF is red) are shown fit to the 15 Å subtomogram average map of the EGFR ECRs on the surface of EVs. Sites of potential N-linked glycosylation are shown in yellow spheres for either N-acetyl glucosamines modeled in the crystal structure or Asparagine residues at consensus glycosylation sites. (*B*) Orthogonal views of the 15 Å map generated from the crystal structure of EGFR dimers bound to EGF as shown in panel *A*). (*C*) Subtomogram average of the intracellular regions of 16 isolated EGFRs with a ribbon the crystal structure of the EGFR asymmetric kinase dimer (RCSB 3GOP) shown with one light pink and one light green kinase subunit.

III, which was observed in single particle averages of EGFR dimers in peptidiscs (27) and molecular dynamics simulations of singly ligated EGFR dimers (58). Although the C-terminal regions of domain IV come into close contact near the membrane, they appear to enter the membrane ~30 Å apart, which is comparable to the distance between the ordered N-terminal residues in an NMR structure of an EGFR TM region dimer (63) and may restrict tilting of EGFR ECRs in the direction parallel to the entry points.

In addition to facilitating structural studies of membrane proteins in host-cell membranes, EVs provide an excellent opportunity to characterize interaction partners of targeted membrane proteins by mass spectrometry. Most mass spectrometric approaches to identification of interaction partners rely on chemical crosslinking or persistence of interactions through detergent lysis and immunoprecipitation, each of which can lead to artifacts (64). Analysis of VLPs or EVs rather than cells greatly reduces the number of background proteins and avoids many of these artifacts, and enrichment of putative interactors can be quantified in comparison to control EVs to provide a measure of confidence (Fig. 2 *E* and *F* and Datasets S1 and S2). Our preliminary mass spectrometric analyses identified many known EGFR interaction partners in EGFR-containing EVs, confirming that VLPs provide an excellent system to characterize the interactome of integral membrane proteins.

In this manuscript, we report development of a VLP-transporter system and use of the EABR tag (39) to stimulate production of EVs containing human integral membrane proteins for structural and functional studies. These approaches differ from previous uses of EVs for structural studies in that vesicle formation is stimulated by engaging ESCRT proteins, the protein of interest is specifically targeted to vesicles and is the most abundant membrane component, and use of sonication or chemical methods to produce vesicles is not needed (36, 44). We show that general features of integral membrane protein structure and organization can be inferred from inspection of individual proteins in tomograms and that proteins as small as the ~150 kD EGFR ECR dimer can be imaged at near nanometer resolution using subtomogram averaging, which is sufficient to reveal domain and subunit organization for most proteins. Mass spectrometric characterization of the proteomes of VLPs containing target proteins also provides a straightforward approach to identification of the interactome of integral membrane proteins. These results demonstrate that transport of human integral membrane proteins to EVs represents a promising approach to facilitate structural and function studies of human integral membrane proteins in cell-derived membranes.

## Methods

**Construction of Transporters and Tagged Membrane Proteins.** Phosphate Buffered Saline (pBS)-CMV-gagpol was a gift from Patrick Salmon (Addgene plasmid #35614; http://n2t.net/addgene:35614; RRID:Addgene_35614, University of Geneva, Switzerland). The polymerase gene, superfluous for VLP production, was deleted from pBS-CMV by PCR (65–67). To construct expression plasmids encoding Strep-tag II binding transporters, a synthetic gene-block encoding the N-terminal region of Influenza A virus Neuraminidase (residues 1 to 47 including transmembrane domain residues 7 to 35) (68) followed by a five-residue Gly-Ser linker, an HRV 3C protease recognition site (47), a five-residue Gly-Ser linker, three FLAG epitopes, a five-residue Gly-Ser linker, and streptavidin (1 to 159 aa) with three mutations that confer higher affinity to Strep-tag II (SA) (69), was inserted into the pBS-CMV backbone. To construct an HA epitope binding transporter, sequences encoding the N-terminal region of Influenza A virus Neuraminidase (residues 1 to 47 including transmembrane domain residues 7 to 35) followed by five-residue Gly-Ser linker, an HRV 3C protease recognition site, a 15-residue Gly-Ser linker, two myc epitopes, an eight-residue Gly-Ser linker, and the anti-HA scFv from pCMV-15F11-HA-mEGFP, which was a gift from Tim Stasevich (Addgene plasmid #129590; http://n2t.net/addgene:129590; RRID:Addgene_129590, Colorado State University, CO) (41), was inserted into the pBS-CMV backbone. The FLAG epitope binding transporter was constructed similarly to the HA transporter except that anti-FLAG heavy and light chain sequences derived a plasmid encoding anti-FLAG M2 antibody (42), which was a gift from Joost Snijder (Addgene plasmid #175359; #175358 http://n2t.net/addgene:175359; RRID:Addgene_175359 or 8, Utrecht University, Netherlands) were used to create the scFv region. Expression plasmids directing expression of

full-length InsR and EGFR with and without N-terminal HA and FLAG epitopes are described elsewhere (70), pcDNA HA-NIS was a gift from Nancy Carrasco (Vanderbilt University, TN). Sequences encoding a Strep-tag II epitope followed by a Gly-Ser linker and a HRV 3C site at the N termini of EGFR, InsR, NIS, and SMO were added to each respective expression plasmids, and versions of these clones with sequences encoding the EABR sequence at their C termini were constructed using the sequence reported by Hoffmann, Bjorkman, and colleagues (39). To construct a negative control for analysis of interactomes by mass spectrometry, the coding sequence of EGFR TM region was cloned into pUE1-TSP-BFLF1, a gift from Britt Glaunsinger (Addgene plasmid #162657; http://n2t.net/addgene:162657; RRID:Addgene_162657, University of California, Berkeley, CA) replacing the BFLF1 sequence by the TM and adding to the N terminus tandemly repeated Strep-tag II epitopes followed by a 5× Gly-Ser linker, an Alfa tag, a 5× Gly-Ser linker, an HRV 3C region and a 5× Gly-Ser linker. The 31 aa TM region is followed by the EABR coding sequence.

**Transfection of CHO, HEK293T, and Expi293F Cells.** CHO-K1 cells (ATCC CCL-61) and HEK293T (ATCC CRL-3216) cells were maintained in DMEM/F12 medium supplemented with 5 to 10% inactivated Fetal Bovine Serum. To test protein expression, cells were seeded in 6-well plates for transfection with PEI (Polyethylenimine "Max" linear, MW 25,000 1 mg/mL) using a 3:1 w/w PEI:DNA ratio for each plasmid to be tested. Cells were washed with Phosphate Buffered Saline (PBS) 24 h post transfection and lysed in Radioimmunoprecipitation assay (RIPA) buffer (50 mM Tris pH 8.0, 150 mM NaCl, 1% v/v NP40, 0.5% w/v sodium deoxycholate, 0.1% w/v SDS) supplemented with 1 mM activated $Na_3VO_4$, one protease inhibitor minitablet (Thermo Scientific) and Benzonase nuclease (Millipore). For VLP production in HEK293T cells, cells were seeded in T175 flasks (4 to 5 flasks) at a 60% confluency, and each flask transfected with 35 μg total plasmid DNA plus 105 μL of PEI. For the viral system, the cotransfection of the MLV *gag* gene together with the receptor (Strep-tagII, HA, or FLAG-tagged) plus the transporter (NA-SA/scfvHA or scfvFLAG) was made with a weight ratio of 1.0:0.4:0.6 (GAG: Transporter: Gene of interest). At 72 h after transfection, conditioned media were collected and adherent cells were lysed with 2 mL of RIPA buffer to be used as an expression control. For transfections in the Expi293F cell line (ThermoFisher), 100 mL of cells at $3 \times 10^6$ cells/mL were transfected with 100 μg of total DNA using the ThermoFisher Expifectamine transfection kit (cat #A14524) according to the manufacturer's instructions. Briefly the DNA was mixed with Opti-Plex Complexation Buffer and the expifectamine reagent and added to cells. 20 h after transfection enhancers 1 and 2 were added, and the conditioned medium collected 4 d after transfection (counting the day of transfection as day 0). For cell-based activation assays, 18 h after transfection cells were washed three times with 2 mL Ham's F12 supplemented with 1 mg/mL BSA and serum starved in this medium for 3 h at 37 °C. Each specific ligand was added in designated wells, 100 ng/mL EGF [purified as described in ref. 71, for 5 min; and 200 nM (1.14 μg/mL) insulin (Novus Biologicals, Cat #NBP1-99193) for 30 min]. Cells were washed with ice-cold phosphate-buffered saline and lysed for 30 min at 4 °C in 250 μL of RIPA buffer.

**Purification of VLP/EVs.** Conditioned media was clarified by two centrifugations at 4,000 x g for 30 min followed by two filtrations using a 0.45 μm filter unit. The media was then ultracentrifuged on a 20% sucrose cushion for 2 h at 100,000 x g using a SW 32 Ti rotor. The vesicle-containing pellets were resuspended in 50 to 2,000 μL of Tris-EDTA-NaCl buffer (TNE) [50 mM Tris-HCl pH 8, 100 mM NaCl, 0.1 mM Ethylenediaminetetraacetic acid (EDTA)] over night, except for Insulin receptor containing vesicles, which were resuspended in 50 mM Tris-HCl pH 7, 300 mM NaCl, 0.2 mM EDTA to avoid vesicle aggregation. Absorbance at 280 nm was used to estimate if the concentration of vesicles was sufficient for cryoEM with an $OD_{280}$ of two being the minimal acceptable value.

The vesicles were purified by affinity purification, using the Strep-tag II fused to the N terminus of the receptors expressed on the vesicles membranes to bind to a SAXT-4flow high-capacity resin (IBA cat#2-5030-025) column. We followed the manufacturer's protocol using 2 mL of resin per 100 mL of conditioned media. The sample was incubated in batch mode overnight at 4 °C followed by rocking overnight in elution buffer at 4 °C. Elution fractions of 1 mL were collected and analyzed by western blot using the following antibodies: rabbit anti-HA Polyclonal (Thermo Fisher Scientific, Cat #PA1-985); rabbit anti-DYKDDDDK (FLAG) Tag Polyclonal Antibody (Thermo Fisher Scientific, Cat #PA1-984B); mouse

anti-NWSHPQFEK Tag (Strep-tag II) Monoclonal Antibody (5A9F9); rabbit anti-EGFR (D38B1, Cell Signaling, Cat #4267), rabbit anti-Insulin Receptor β-chain (Millipore Sigma, Cat #07-724); rabbit Monoclonal Antibody anti-Smoothened (E6Z5T, Cell Signaling, Cat #92981). Rabbit anti-phospho-EGFR pTyr1068 antibody (Thermo Fisher Scientific, Cat #44-788G); mouse anti-phosphotyrosine clone 4G10 (EMD Millipore, Cat #05-321); rabbit anti-phospho-IR β Tyr1150/1151 (Cell Signaling Technology, Cat #2969). Rabbit anti-β-Actin (Cell Signaling Technology, Cat #4968) and rabbit anti-Hsp90α (Cell Signaling Technology, Cat #4877) were used to calibrate protein loading concentrations. Goat anti-rabbit-680RD (Li-Cor, Cat #926-68071) and Goat anti-mouse IgG2b-800CW (Li-Cor, Cat #926-32352) were used as secondary antibodies and detected using a Li-Cor Odyssey Clx Near IR imaging system.

Receptor-containing affinity-column elution fractions were combined and ultracentrifuged through a 20% sucrose cushion in PBS for 2 h at 100,000 x g using a Beckman SW 32 Ti rotor. Pellets were resuspended in 50 to 200 μL of TNE overnight with gentle agitation at 4 °C. The concentrated vesicles were quantified by spectrophotometry by absorbance at 280 nm and screened by negative stain electron microscopy using Formvar carbon supported copper grids, 300 mesh (EM Sciences #FCF300-Cu-50 241141). Four μL of sample at $\sim OD_{280} \geq 2.0$ was applied to the grid. After 2 min, the sample was blotted and immediately washed twice in water for 30 s before incubation with 4 μL of 2% Uranyl Acetate at pH 4.5 for 45 s. The grid was then blotted and air-dried. Images were collected using an FEI JEOL NEOARM scanning transmission electron microscope operated at 200 kV equipped with an EDS detector. The vesicles were then aliquoted, and flash frozen with liquid nitrogen, stored at −80 °C. In vitro phosphorylation of the EVs was tested by incubating 10 μL of purified EVs with 1 mM adenosine triphosphate, 1 mM $Na_3VO_4$, 20 nm HEPES, 50 mM $MgCl_2$ with or without of 1 μg/mL EGF incubated at room temperature for 5 min. Loading buffer was added and samples analyzed by western blot.

**Mass Spectrometry Sample Preparation.** VLPs or EVs in TNE buffer (50 mM Tris-Cl pH 8.0, 200 mM NaCl, 0.1 mM EDTA) were prepared for mass spectrometry using the membrane protein-optimized method of Lin et al. (72). Briefly, an equal volume of 4% SDS was added (for 2% final concentration), samples were boiled 5 min and proteins precipitated with six volumes ice-cold acetone for at least 4 h 4 °C. The precipitate was pelleted at 16,000× g for 15 min at 4 °C, the supernatant was discarded, and the pellet washed twice with 400 μL cold acetone and recentrifuged as before. Care was taken to remove all but ~20 μL of supernatant in each cycle to preserve the delicate pellet. The washed pellet was air dried and resuspended in 100 μL 1% sodium deoxycholate, 50 mM ammonium bicarbonate with bath sonication (2× 10 min). Proteins were reduced (TCEP to 5 mM, 56 °C, 45 min) and alkylated (iodoacetamide 25 mM, 45 min room temperature in the dark). Alkylation was quenched with 12 mM Dithiothreitol and proteins digested overnight at 37 °C with 0.5 to 1 μg MS-grade trypsin (Pierce #90058). Trypsin was inactivated and sodium deoxycholate precipitated by addition of formic acid to 1% followed by centrifugation at 16,000× g at 4 °C for 10 min. The supernatant was transferred to a fresh tube and the volume adjusted to 250 μL prior to ultrafiltration in a prewashed Vivaspin500 (Sartorius) or AmiconUltra (Millipore) 10 kDa filtration unit. Filtrate was dried and resuspended in 20 μL 0.1% Trifluoroacetic acid (TFA) for desalting using a ZipTip (Millipore #ZTC18S096), eluted in 10 μL 50% acetonitrile and 0.1% TFA, dried, and resuspended in 18 to 20 μL 5% acetonitrile, 0.1% formic acid for Liquid Chromatography/MS. Two to three 5 μL injections of each sample were performed on a minimum of two replicate samples for each protein of interest.

**Mass Spectrometry Data Collection and Analysis.** Mass spectra were collected using a Thermo Orbitrap Fusion Lumos Tribrid mass spectrometer and a data-dependent 75-min top speed collection method with a 60 min 3 to 40% acetonitrile gradient, dynamic exclusion after one observation for 15 s, and stepped HCD (27/30/33). RAW files were individually processed in Proteome Discoverer 2.5 using the PWF Tribrid_Basic_SequestHT workflow with the Percolator node for PSM validation and the following settings: trypsin digestion with up to two missed cleavages, static carbamidomethyl modification of cysteine, and dynamic modifications of oxidized methionine, and protein N-terminal modifications of Met-loss, Acetyl, or Met-loss + Acetyl. For spectral searches, FASTA files containing sequences of the synthetic tagged transporter and protein of interest were included along with the standard Uniprot human proteome and common

contaminants. Data including FASTA files are available from the MassIVE data repository # MSV000096822. Initially, each RAW file was processed to produce an msf file, and the msf files from samples to be compared were reprocessed as needed using the CWF_Basic workflow with Merge Mode "Do Not Merge" to create a single Consensus file for comparative analysis. Results were filtered to require FDR ≤1% and to remove contaminants and proteins identified by a single PSM. For comparing relative protein abundances in control VLP/EVs vs. VLP/EVs containing the protein of interest, differential protein enrichment was computed using the RUVr edgeR-quasi-likelihood model implemented in Degust (73), requiring a minimum count of two PSMs in at least two samples, and normalizing by Trimmed Mean of M-values. Absolute abundances of membrane proteins were estimated using the label-free iBAQ analysis implemented in MaxQuant, identifying transmembrane proteins based on Uniprot annotations, and computing histograms with Perseus. Estimated molar fractions were computed using the riBAQ method (50).

**Cryo-ET Sample Preparation.** Addition of EGF to EVs was carried out by adding 3 µL of 33 µg/mL EGF to 20 µL of concentrated EVs followed by incubation at room temperature for 5 min and 30 min on ice. Concentrated EVs with or without added EGF were mixed with 10-nm colloidal gold (in PBS solution) in a 10:1 ratio. 3 µL of the solution was then added to a glow-discharged ultrafoil gold grid (Quantifoil 2/2, 200 mesh, Ted Pella #687-200-AU-50). Grids were plunge frozen into liquid ethane by double-side blotting using a Vitrobot cryoplunger (Thermo Fisher) and stored in liquid nitrogen until imaging.

**Cryo-ET Data Collection.** Cryo-ET data collection was performed essentially as described previously (31) and software used in this project was curated by SBGrid (74). Cryogrids containing the EVs were loaded into an FEI Titan Krios transmission electron microscope operated at 300 kV, and images were recorded on a Gatan K3 Biocontinuum Imaging Filter (Gatan) direct detection camera in counting mode with a 20 eV energy slit in zero-loss mode. Tomographic tilt series between −60° and +60° were collected with serialEM (75) using a dose-symmetric scheme (76) with a 3° angular increment. A total dose of 120 e$^-$/Å$^2$ per tilt series was distributed evenly among 41 tilt images. The nominal magnification was 53,000×, giving a pixel size of 1.69 Å on the specimen. The defocus range was between −4 µm and −5 µm and eight frames were saved for each tilt angle. All data acquisition parameters are listed in *SI Appendix*, Table S1.

For cryo-ET data collection of the EGFR without EGF ligand sample, sample preparation and data collection were carried out as described for EGFR with EGF except that EGF was not added to the sample and images were recorded on a Falcon 4i camera with 10 eV energy slit in zero-loss mode. The pixel size is 1.82 Å and the defocus range was between −4 to −6 µm.

**Cryo-ET Data Processing.** The preprocessing of the tilt series was done in RELION5 (77, 78) using *relion --tomo*. The movies and mdoc files were imported, the frames were motion-corrected using MotionCor2 (79) and the contrast transfer function (CTF) was measured using the CTFFIND4 package (80). After poor-quality tilt images were excluded, the tilt series stacks were aligned automatically with the 10-nm fiducials, an IMOD (81) function adapted within RELION5. The 10-nm gold fiducials were removed using *imodfindbeads, ccderaser,* and *newstack* functions from the motion-corrected micrographs. Specifically, *imodfindbeads* locates regions with MinRelativeStrength 0.05 and diameter of 60 pixels (~10 nm) and assigns them as gold fiducial sites. Then *ccderaser* replaces the assigned pixels with gray values using ExpandCircleIterations 3 and PolynomialOrder -1 in the IMOD program. The final tomogram reconstruction was carried out using the gold fiducial-based alignment and the fiducial-erased micrographs at 4× binning. For better visualization, tomograms were low-pass filtered to 50 Å using *e2proc3d.py* function from EMAN2 (82) and tomographic slices were visualized with IMOD (81).

**Extraction of EGFR Dimers from Tomograms.** The initial steps of subtomogram alignment and averaging were done with the subTOM package (Dustin Morado subTOM: https://github.com/DustinMorado/subTOM), which was originally implemented using MATLAB (MathWorks) scripts derived from the TOM (83) and AV3 (84) packages as described previously (31).

To generate an initial template model of the EGFR protein from the EV surface, 160 EGFR particles were manually picked using a two-point picking strategy from seven EVs that were down-scaled by 4× binning of the voxels (pixel size of 6.76 Å) (*SI Appendix*, Fig. S12). The 160 EGFR particles' initial Euler angles (2 out of 3)

were determined based on the vector between two points, one on the head of the EGFR and one on the membrane where the EGFR anchors, respectively. The 160 EGFR were iteratively aligned to one another for three iterations with a soft-edge cylinder mask covering the EGFR ectodomain, revealing a twofold symmetrical EGFR dimer. Hereafter, this template and twofold symmetry was used during the subsequent alignment and averaging process.

We tried to automatically locate the rest of the EGFR dimers on all the EVs with the existing initial template model by applying a previous oversampled spherical grid of points approach that worked for SARS-CoV-2 spike protein (31). However, due to the much-lower molecular weight (150 kDa vs. 500 kDa or greater), lower-symmetry (C2 vs. C6), lack of an ordered lattice, and the density of EGFR proteins on the EV surface, automatic template matching the EGFR dimers on EVs failed.

We then manually picked 1,602 EGFR dimers from 22 tomograms using the two-point approach used earlier to determine the initial template model. Subtomograms were aligned against the low-resolution template (from the above average of 1,602 EGFR dimers). Visual inspection of the tomograms using the Place Object Chimera Plugin (60) confirmed that subtomograms selected in this manner corresponded to EGFR dimers on the EV surface. Iterative alignment and averaging were performed at a binning of four (pixel size of 6.76 Å) in subTOM and resulted in a 32 Å averaged dimer. Subtomograms were divided into two halves based on the tomogram number. From this point on the two halves were processed independently in RELION5 (78).

**Subtomogram Averaging of EGFR in RELION.** Subsequent processing was performed in RELION5 (77, 78) as described in ref. 31. For this purpose, subtomograms were reconstructed from the gold fiducial-removed micrographs after motion correction. Using dedicated python scripts (motl2relion), the EGFR positions in the 3D tomograms from subTOM were converted into 2D positions and defocus values in the corresponding tilt series images, as well as Euler angles in the RELION starfile convention. Individual subtomograms were reconstructed at a 3× down-scaled pixel size of 5.07 Å in a cropped box size of 96 voxels.

Standard 3D autorefinement was performed with C2 symmetry and a soft-edged mask around the EGFR dimers, using a 60 Å low-pass filtered map generated from subTOM alignment parameters as initial reference. 3D classification was applied to sort the particle heterogeneity, and 843 of the 1,602 particles were kept for further refinement. The final alignment and averaging were carried out with unbinned subtomograms and a box size of 192 cropped from box size of 256. Finally, a 15 Å consensus map was calculated for the EGFR dimers (*SI Appendix*, Fig. S12).

**Subtomogram Averaging of ICR.** The averaging process for the ICR is similar to the EGFR ectodomain, with a two-point approach mentioned above. Because the crowded ICR particles are generally too noisy to be resolved and averaged, we chose to pick only isolated and well-defined ICR particles for averaging, and an average was generated from 16 particles. Due to the low number of particles and small protein size, we did not proceed with iterative alignment.

**Quantification of EV Diameter.** For EV diameter measurements, EV diameters were quantified from cryo-ET tomographic sections that were 4× binned and low-pass filtered to 50 Å (EMAN2 *e2proc3d.py*) (82) for better visualization. Quantification of EV diameter was done using IMOD by adding open contour points on each complete EV (n = 167) and the diameters were calculated (*SI Appendix*, Fig. S8). Note, incomplete EVs were not considered for quantification. The *imodinfo* utility was used to extract the virion diameter information from the saved model files.

**Segmentation of EV and EGFR.** Density map segmentation and surface rendering were conducted using the Volume Tracer and Color Zone tools in UCSF ChimeraX (85). Markers were first added in ChimeraX to designate the ECR, membrane, and ICR regions within the tomograms. These regions were then segmented into different maps using the Color Zone tool, with each region assigned a unique color for clear visualization.

**Radial Average Density Profile.** The "Radial Profile Angle" plugin in ImageJ (86) was employed to calculate the radial average density profile of regions with and without ICR and ECR in both EGF liganded and no EGF EVs. The plugin was used to identify the center, define the starting angle, and set an integration angle of 25° for each region. The radial average density was then calculated, and the resulting data were exported to MATLAB for further analysis.

1. H. M. Berman *et al.*, The protein data bank. *Nucleic Acids Res.* **28**, 235–242 (2000).
2. K. Cai, X. Zhang, X.-C. Bai, Cryo-electron microscopic analysis of single-pass transmembrane receptors. *Chem. Rev.* **122**, 13952–13988 (2022).
3. R. Reis, I. Moraes, Structural biology and structure-function relationships of membrane proteins. *Biochem. Soc. Trans.* **47**, 47–61 (2019).
4. K. M. Ferguson *et al.*, EGF activates its receptor by removing interactions that autoinhibit ectodomain dimerization. *Mol. Cell.* **11**, 507–517 (2003).
5. A. W. Burgess *et al.*, An open-and-shut case? Recent insights into the activation of EGF/ErbB receptors. *Mol. Cell.* **12**, 541–552 (2003).
6. H. Ogiso *et al.*, Crystal structure of the complex of human epidermal growth factor and receptor extracellular domains. *Cell* **110**, 775–787 (2002).
7. T. P. J. Garrett *et al.*, Crystal structure of a truncated epidermal growth factor receptor extracellular domain bound to transforming growth factor alpha. *Cell* **110**, 763–773 (2002).
8. X. Zhang, J. Gureasko, K. Shen, P. A. Cole, J. Kuriyan, An allosteric mechanism for activation of the kinase domain of epidermal growth factor receptor. *Cell* **125**, 1137–1149 (2006).
9. J. Stamos, M. X. Sliwkowski, C. Eigenbrot, Structure of the epidermal growth factor receptor kinase domain alone and in complex with a 4-anilinoquinazoline inhibitor. *J. Biol. Chem.* **277**, 46265–46272 (2002).
10. Y. Yarden, J. Schlessinger, Epidermal growth factor induces rapid, reversible aggregation of the purified epidermal growth factor receptor. *Biochemistry* **26**, 1443–1451 (1987).
11. N. Kozer *et al.*, Evidence for extended YFP-EGFR dimers in the absence of ligand on the surface of living cells. *Phys. Biol.* **8**, 066002 (2011).
12. P. Liu *et al.*, Investigation of the dimerization of proteins from the epidermal growth factor receptor family by single wavelength fluorescence cross-correlation spectroscopy. *Biophys. J.* **93**, 684–698 (2007).
13. J. L. Macdonald, L. J. Pike, Heterogeneity in EGF-binding affinities arises from negative cooperativity in an aggregating system. *Proc. Natl. Acad. Sci. U.S.A.* **105**, 112–117 (2008).
14. M. Martin-Fernandez, D. T. Clarke, M. J. Tobin, S. V. Jones, G. R. Jones, Preformed oligomeric epidermal growth factor receptors undergo an ectodomain structure change during signaling. *Biophys. J.* **82**, 2415–2427 (2002).
15. T. Moriki, H. Maruyama, I. N. Maruyama, Activation of preformed EGF receptor dimers by ligand-induced rotation of the transmembrane domain. *J. Mol. Biol.* **311**, 1011–1026 (2001).
16. P. Nagy, J. Claus, T. M. Jovin, D. J. Arndt-Jovin, Distribution of resting and ligand-bound ErbB1 and ErbB2 receptor tyrosine kinases in living cells using number and brightness analysis. *Proc. Natl. Acad. Sci. U.S.A.* **107**, 16524–16529 (2010).
17. T. W. Gadella, T. M. Jovin, Oligomerization of epidermal growth factor receptors on A431 cells studied by time-resolved fluorescence imaging microscopy. A stereochemical model for tyrosine kinase receptor activation. *J. Cell Biol.* **129**, 1543–1558 (1995).
18. S. Saffarian, Y. Li, E. L. Elson, L. J. Pike, Oligomerization of the EGF receptor investigated by live cell fluorescence intensity distribution analysis. *Biophys. J.* **93**, 1021–1031 (2007).
19. K. C. Mudumbi *et al.*, Distinct interactions stabilize EGFR dimers and higher-order oligomers in cell membranes. *Cell Rep.* **43**, 113603 (2024).
20. A. H. A. Clayton, S. G. Orchard, E. C. Nice, R. G. Posner, A. W. Burgess, Predominance of activated EGFR higher-order oligomers on the cell surface. *Growth Factors* **26**, 316–324 (2008).
21. A. H. A. Clayton *et al.*, Ligand-induced dimer-tetramer transition during the activation of the cell surface epidermal growth factor receptor-A: A multidimensional microscopy analysis. *J. Biol. Chem.* **280**, 30392–30399 (2005).
22. K. J. Wilson, J. L. Gilmore, J. Foley, M. A. Lemmon, D. J. Riese, Functional selectivity of EGF family peptide growth factors: Implications for cancer. *Pharmacol. Ther.* **122**, 1–8 (2009).
23. C. J. Childs *et al.*, Epiregulin creates a developmental niche for spatially organized human intestinal enteroids. *JCI Insight* **8**, 1–18 (2023), 10.1172/jci.insight.165566.
24. S.-H. Lee *et al.*, Amphiregulin switches progenitor cell fate for lineage commitment during gastric mucosal regeneration. *Gastroenterology* **167**, 469–484 (2024).
25. J. K. L. Sinclair, A. S. Walker, A. E. Doerner, A. Schepartz, Mechanism of allosteric coupling into and through the plasma membrane by EGFR. *Cell Chem. Biol.* **25**, 857–870.e7 (2018).
26. N. F. Endres *et al.*, Conformational coupling across the plasma membrane in activation of the EGF receptor. *Cell* **152**, 543–556 (2013).
27. Y. Huang *et al.*, A molecular mechanism for the generation of ligand-dependent differential outputs by the epidermal growth factor receptor. *Elife* **10**, 1–32 (2021), 10.7554/eLife.73218.
28. D. M. Freed *et al.*, EGFR ligands differentially stabilize receptor dimers to specify signaling kinetics. *Cell* **171**, 683–695.e18 (2017).
29. R. Trenker, D. Diwanji, T. Bingham, K. A. Verba, N. Jura, Structural dynamics of the active HER4 and HER2/HER4 complexes is finely tuned by different growth factors and glycosylation. *Elife* **12**, 1–27 (2024), 10.7554/eLife.92873.
30. D. Diwanji *et al.*, Structures of the HER2-HER3-NRG1β complex reveal a dynamic dimer interface. *Nature* **600**, 339–343 (2021).
31. Z. Ke *et al.*, Structures and distributions of SARS-CoV-2 spike proteins on intact virions. *Nature* **588**, 498–502 (2020).
32. H. Yao *et al.*, Molecular architecture of the SARS-CoV-2 virus. *Cell* **183**, 730–738.e13 (2020).
33. V. S. Mandala, R. MacKinnon, The membrane electric field regulates the PIP2-binding site to gate the KCNQ1 channel. *Proc. Natl. Acad. Sci. U.S.A.* **120**, e2301985120 (2023).
34. W. Zheng, P. Chai, J. Zhu, K. Zhang, High-resolution in situ structures of mammalian respiratory supercomplexes. *Nature* **631**, 232–239 (2024).
35. J. M. Di Trani *et al.*, Cryo-EM of native membranes reveals an intimate connection between the Krebs cycle and aerobic respiration in mycobacteria. *Proc. Natl. Acad. Sci. U.S.A.* **122**, e2423761122 (2025).
36. X. Tao, C. Zhao, R. MacKinnon, Membrane protein isolation and structure determination in cell-derived membrane vesicles. *Proc. Natl. Acad. Sci. U.S.A.* **120**, e2302325120 (2023).
37. S. Nooraei *et al.*, Virus-like particles: Preparation, immunogenicity and their roles as nanovaccines and drug nanocarriers. *J. Nanobiotechnol.* **19**, 59 (2021).
38. A. Zeltins, Construction and characterization of virus-like particles: A review. *Mol. Biotechnol.* **53**, 92–107 (2013).
39. M. A. G. Hoffmann *et al.*, ESCRT recruitment to SARS-CoV-2 spike induces virus-like particles that improve mRNA vaccines. *Cell* **186**, 2380–2391.e9 (2023).
40. S. Eyckerman *et al.*, Trapping mammalian protein complexes in viral particles. *Nat. Commun.* **7**, 11416 (2016).
41. N. Zhao *et al.*, A genetically encoded probe for imaging nascent and mature HA-tagged proteins in vivo. *Nat. Commun.* **10**, 2947 (2019).
42. J. W. Beugelink, E. Sweep, B. J. C. Janssen, J. Snijder, M. F. Pronker, Structural basis for recognition of the FLAG-tag by anti-FLAG M2. *J. Mol. Biol.* **436**, 168649 (2024).
43. S. Banskota *et al.*, Engineered virus-like particles for efficient in vivo delivery of therapeutic proteins. *Cell* **185**, 250–265.e16 (2022).
44. T. Zeev-Ben-Mordehai, D. Vasishtan, C. A. Siebert, C. Whittle, K. Grünewald, Extracellular vesicles: A platform for the structure determination of membrane proteins by Cryo-EM. *Structure* **22**, 1687–1692 (2014).
45. H. M. Miettinen, J. K. Rose, I. Mellman, Fc receptor isoforms exhibit distinct abilities for coated pit localization as a result of cytoplasmic domain heterogeneity. *Cell* **58**, 317–327 (1989).
46. T. G. Schmidt, J. Koepke, R. Frank, A. Skerra, Molecular interaction between the Strep-tag affinity peptide and its cognate target, streptavidin. *J. Mol. Biol.* **255**, 753–766 (1996).
47. R. T. Libby *et al.*, Human rhinovirus 3C protease: Cloning and expression of an active form in *Escherichia coli*. *Biochemistry* **27**, 6262–6268 (1988).
48. T. G. M. Schmidt, A. Skerra, The Strep-tag system for one-step purification and high-affinity detection or capturing of proteins. *Nat. Protoc.* **2**, 1528–1535 (2007).
49. B. Schwanhäusser *et al.*, Global quantification of mammalian gene expression control. *Nature* **473**, 337–342 (2011).
50. J.-B. Shin *et al.*, Molecular architecture of the chick vestibular hair bundle. *Nat. Neurosci.* **16**, 365–374 (2013).
51. P. Wee, Z. Wang, Epidermal growth factor receptor cell proliferation signaling pathways. *Cancers (Basel)* **9**, 52 (2017), 10.3390/cancers9050052.
52. P. O. Byrne, K. Hristova, D. J. Leahy, EGFR forms ligand-independent oligomers that are distinct from the active state. *J. Biol. Chem.* **295**, 13353–13362 (2020).
53. Y.-T. Liu *et al.*, Isotropic reconstruction for electron tomography with deep learning. *Nat. Commun.* **13**, 6482 (2022).
54. M. Red Brewer *et al.*, The juxtamembrane region of the EGF receptor functions as an activation domain. *Mol. Cell.* **34**, 641–651 (2009).
55. N. Jura *et al.*, Mechanism for activation of the EGF receptor catalytic domain by the juxtamembrane segment. *Cell* **137**, 1293–1307 (2009).
56. J. Abramson *et al.*, Accurate structure prediction of biomolecular interactions with AlphaFold3. *Nature* **630**, 493–500 (2024).
57. C. Lu *et al.*, Structural evidence for loose linkage between ligand binding and kinase activation in the epidermal growth factor receptor. *Mol. Cell. Biol.* **30**, 5432–5443 (2010).
58. A. Arkhipov *et al.*, Architecture and membrane interactions of the EGF receptor. *Cell* **152**, 557–569 (2013).
59. S. McLaughlin, S. O. Smith, M. J. Hayman, D. Murray, An electrostatic engine model for autoinhibition and activation of the epidermal growth factor receptor (EGFR/ErbB) family. *J. Gen. Physiol.* **126**, 41–53 (2005).
60. K. Qu *et al.*, Structure and architecture of immature and mature leukemia virus capsids. *Proc. Natl. Acad. Sci. U.S.A.* **115**, E11751–E11760 (2018).
61. O. Kovtun *et al.*, Structure of the membrane-assembled retromer coat determined by cryo-electron tomography. *Nature* **561**, 561–564 (2018).
62. C. E. Coupland *et al.*, High-resolution electron cryomicroscopy of V-ATPase in native synaptic vesicles. *Science* **385**, 168–174 (2024).
63. E. V. Bocharov *et al.*, The conformation of the epidermal growth factor receptor transmembrane domain dimer dynamically adapts to the local membrane environment. *Biochemistry* **56**, 1697–1705 (2017).
64. X. Liu, L. Abad, L. Chatterjee, I. M. Cristea, M. Varjosalo, Mapping protein-protein interactions by mass spectrometry. *Mass Spectrom. Rev.*, 10.1002/mas.21887 (2024).

65. B. Bellier *et al.*, A thermostable oral SARS-CoV-2 vaccine induces mucosal and protective immunity. *Front. Immunol.* **13**, 837443 (2022).

66. M. Kirchmeier *et al.*, Enveloped virus-like particle expression of human cytomegalovirus glycoprotein B antigen induces antibodies with potent and broad neutralizing activity. *Clin. Vaccine Immunol.* **21**, 174–180 (2014).

67. J. L. Martin, S. Cao, J. O. Maldonado, W. Zhang, L. M. Mansky, Distinct particle morphologies revealed through comparative parallel analyses of retrovirus-like particles. *J. Virol.* **90**, 8074–8084 (2016).

68. S. J. Kaczmarczyk, K. Sitaraman, H. A. Young, S. H. Hughes, D. K. Chatterjee, Protein delivery using engineered virus-like particles. *Proc. Natl. Acad. Sci. U.S.A.* **108**, 16998–17003 (2011).

69. I. P. Korndörfer, A. Skerra, Improved affinity of engineered streptavidin for the Strep-tag II peptide is due to a fixed open conformation of the lid-like loop at the binding site. *Protein Sci.* **11**, 883–893 (2002).

70. M. Gonzalez-Magaldi, J. M. McCabe, H. N. Cartwright, N. Sun, D. J. Leahy, Conserved roles for receptor tyrosine kinase extracellular regions in regulating receptor and pathway activity. *Biochem. J.* **477**, 4207–4220 (2020).

71. C. Qiu *et al.*, In vitro enzymatic characterization of near full-length EGFR in activated and inhibited states. *Biochemistry* **48**, 6624–6632 (2009).

72. Y. Lin *et al.*, Development and evaluation of an entirely solution-based combinative sample preparation method for membrane proteomics. *Anal. Biochem.* **432**, 41–48 (2013).

73. D. R. Powell, Degust: Interactive RNA-seq analysis. https://doi.org/10.5281/zenodo.3258932. Accessed 28 October 2024.

74. A. Morin *et al.*, Collaboration gets the most out of software. *Elife* **2**, e01456 (2013).

75. D. N. Mastronarde, Automated electron microscope tomography using robust prediction of specimen movements. *J. Struct. Biol.* **152**, 36–51 (2005).

76. W. J. H. Hagen, W. Wan, J. A. G. Briggs, Implementation of a cryo-electron tomography tilt-scheme optimized for high-resolution subtomogram averaging. *J. Struct. Biol.* **197**, 191–198 (2017).

77. J. Zivanov *et al.*, A Bayesian approach to single-particle electron cryo-tomography in RELION-4.0. *Elife* **11**, 1–22 (2022), 10.7554/eLife.83724.

78. A. Burt *et al.*, An image processing pipeline for electron cryo-tomography in RELION-5. *FEBS Open Bio.* **14**, 1788–1804 (2024).

79. S. Q. Zheng *et al.*, MotionCor2: Anisotropic correction of beam-induced motion for improved cryo-electron microscopy. *Nat. Methods.* **14**, 331–332 (2017).

80. A. Rohou, N. Grigorieff, CTFFIND4: Fast and accurate defocus estimation from electron micrographs. *J. Struct. Biol.* **192**, 216–221 (2015).

81. J. R. Kremer, D. N. Mastronarde, J. R. McIntosh, Computer visualization of three-dimensional image data using IMOD. *J. Struct. Biol.* **116**, 71–76 (1996).

82. J. G. Galaz-Montoya, J. Flanagan, M. F. Schmid, S. J. Ludtke, Single particle tomography in EMAN2. *J. Struct. Biol.* **190**, 279–290 (2015).

83. S. Nickell *et al.*, TOM software toolbox: Acquisition and analysis for electron tomography. *J. Struct. Biol.* **149**, 227–234 (2005).

84. F. Förster, O. Medalia, N. Zauberman, W. Baumeister, D. Fass, Retrovirus envelope protein complex structure in situ studied by cryo-electron tomography. *Proc. Natl. Acad. Sci. U.S.A.* **102**, 4729–4734 (2005).

85. E. F. Pettersen *et al.*, UCSF ChimeraX: Structure visualization for researchers, educators, and developers. *Protein Sci.* **30**, 70–82 (2021).

86. C. A. Schneider, W. S. Rasband, K. W. Eliceiri, NIH Image to ImageJ: 25 years of image analysis. *Nat. Methods* **9**, 671–675 (2012).

87. Z. Ke, D. Leahy, Data from "Structure and organization of full-length epidermal growth factor receptor in extracellular vesicles by cryo-electron tomography." Electron Microscopy Data Bank. https://www.ebi.ac.uk/emdb/EMD-49404. Deposited 24 February 2025.

88. E. Marcotte, O. Papoulas, D. Leahy, Structure and organization of full-length epidermal growth factor receptor in extracellular vesicles by cryo-electron tomography. MassIVE. https://massive.ucsd.edu/ProteoSAFe/dataset.jsp?task=3faee72f935b4d01be10aeac8ec19d92. Deposited 25 November 2024.